Nuclear-spin-relaxation mechanisms of nuclear-ordered bcc solid ^{3}He in the low-field phase

Yutaka Sasaki, Taku Matsushita, Takao Mizusaki, and Akira Hirai
Department of Physics, Kyoto University, Kyoto 606, Japan
(Received 8 April 1991)

cw-NMR experiments have been performed on nuclear-ordered bcc solid ^{3}He in the low-field phase. We measured the cw-NMR spectrum and its linewidth as a function of external magnetic fields and temperatures for single-crystal samples having various crystal orientations relative to the external field. From the data on the external magnetic field dependence of the linewidth, we found clear evidence of the field region where the three-magnon process is forbidden. We compared our experimental data with the recent theoretical calculation by Ohmi and Tsubota on the lifetime of a uniform spin precession via the three- and four-magnon processes. The agreement is satisfactory. We estimated the size and distribution of the magnetic domains by using an NMR imaging technique. The size of a magnetic domain was found to be comparable to that of a whole crystal. We found some evidence that a crystal in the ordered phase was distorted (on order of 10^{-3}) uniaxially due to magnetostriction. In some crystal samples, we observed a peculiar field dependence of the antiferromagnetic resonance frequency Ω_0.

I. INTRODUCTION

Nuclear-ordered bcc solid ^{3}He in the low-field phase offers a unique opportunity to study nuclear-spin dynamics in a nuclear-ordered antiferromagnet with a uniaxial anisotropy. The antiferromagnet has a spin structure that is usually called the "$U2D2$" spin structure.[1,2] The anisotropy axis $\boldsymbol{l}$ is along the (100) axis of the bcc lattice. Spins are aligned ferromagnetically in planes perpendicular to $\boldsymbol{l}$, and have an antiferromagnetic sequence of up-up-down-down along $\boldsymbol{l}$. The equations that describe the uniform spin dynamics for this antiferromagnet (OCF equations) were proposed by Osheroff *et al.*[1] to explain their observed resonance spectrum of the cw-NMR. The OCF equations are written as follows:

$$\dot{S}=\gamma\mathbf{S}\times\mathbf{H}_0-\frac{\chi}{\gamma^2}\Omega_0^2(\hat{\mathbf{d}}\cdot\boldsymbol{l})(\hat{\mathbf{d}}\times\boldsymbol{l}) , \tag{1a}$$

$$\dot{\hat{\mathbf{d}}}=\gamma\hat{\mathbf{d}}\times\left[\mathbf{H}_0-\frac{\gamma}{\chi}\mathbf{S}\right] , \tag{1b}$$

where $\gamma\mathbf{S}$ is the magnetization, $\mathbf{H}_0$ is the external magnetic field, $\mathbf{d}$ is the unit vector of the sublattice magnetization (the order parameter), Ω_0 is the zero-field antiferromagnetic resonance frequency [Ω_0 depends on temperature, and a notation $\Omega_0(T)$ will be used when the temperature dependence of Ω_0 should be emphasized], γ is the gyromagnetic ratio of ^{3}He nuclear spin, and χ is the transverse susceptibility. The resonance frequencies from these OCF equations can be solved in the linear regime around its equilibrium configuration, where $\hat{\mathbf{d}}\perp\boldsymbol{l}$ and $\hat{\mathbf{d}}\perp\mathbf{H}_0$. There are two modes of resonance, ω_+ and ω_-. The mode of ω_+ is called the upper mode and that of ω_- the lower mode.

$$\omega_\pm^2=\tfrac{1}{2}[\omega_L^2+\Omega_0^2\pm\sqrt{(\omega_L^2-\Omega_0^2)^2+4\omega_L^2\Omega_0^2\cos^2\theta}] , \tag{2}$$

where $\omega_L=\gamma H_0$ is the Larmor frequency at $\mathbf{H}_0$ and θ is the angle between $\boldsymbol{l}$ and $\mathbf{H}_0$. One of the special features of the spin dynamics in this system is that the nuclear dipolar interaction plays a major role in the spin dynamics because of the uniaxial symmetry of the nuclear ordering. The exchange spin Hamiltonian, which leads to the $U2D2$ spin structure, has been studied extensively.[3] In addition, all the parameters needed to specify this system, such as the transverse susceptibility, χ,[4] spin-wave velocity, c,[5] and strength of the nuclear dipolar interaction, Ω_0,[1] have been determined with high accuracy. Beside the fact that nuclear-ordered solid ^{3}He is one of few examples of nuclear-ordered systems,[6] a study of the spin relaxation in this system would be the clearest test for spin-relaxation mechanisms without any unknown parameters.

Kusumoto *et al.*[7] studied the nonlinear spin dynamics of this antiferromagnet by pulsed NMR methods. They found anomalous behavior of a free induction decay signal after a pulsed rf field. In connection with this experiment, Tsubota, Ohmi, and Tsuneto[8-11] studied this antiferromagnet theoretically and proposed several spin relaxation mechanisms. Tsubota and Tsuneto[8,9] also studied the chaotic spin motion of this system after a strong rf pulse. They introduced phenomenologically a relaxation term to the OCF equations and showed that energy dissipation was enhanced drastically once the chaotic motion was induced. Ohmi *et al.*[10] studied the instability of a homogeneous precession of magnetization in the high-field limit. They predicted that the homogeneous precession for $\cos^2\theta>\frac{1}{5}$ becomes unstable against the excitation of a nonuniform spin wave mode when the magnetization is tipped away from the equilibrium configuration by application of a strong rf field. Tsubota *et al.*[11] studied the structure of magnetic domain walls and calculated the spin wave transmission across the domain wall. According to their calculation a spin wave at a long wavelength limit is reflected almost perfectly at the domain wall in the high-field limit. After this experi-

mental and theoretical work it is now highly desirable to find out what the intrinsic relaxation mechanisms are in nuclear-ordered solid ^{3}He. In order to clarify the relaxation mechanisms of nuclear-ordered ^{3}He in the low-field phase, we have made extensive measurements of the absorption linewidth by cw-NMR. Preliminary results were reported at several conferences.[12–14]

II. EXPERIMENTAL APPARATUS AND PROCEDURES

Figure 1 shows our apparatus. In order to make a sample crystal without any strain, we grew crystals from the liquid. For this purpose we used a conventional compressional cell (*d*) to pressurize the liquid to form solid. The compressional cell was similar to that used by Kusumoto *et al.*,[7] except that there was no heater in this experiment to initiate solid formation in the NMR sample cell (*a*). The compressional cell was made of copper except for the bellows and contained a sintered silver heat exchanger whose surface area was about 200 m^2 inside the ^{3}He space. This device was attached to the nuclear demagnetization stage (*f*) which consisted of 32 moles of copper in an 8-T magnetic field. After precooling this nuclear stage down to 10 mK in 5 days and demagnetizing in 20 h, the ^{3}He sample could be kept below 0.9 mK for more than 10 days for an actual experimental run. The NMR tail piece, (*a*) and (*b*), was made of epoxy (Stycast 1266), and was connected to the bottom of the compressional device (*d*). The NMR chamber for the solid He sample, (*a*), had a hemicylindrical shape with a horizontal flat surface at the bottom. A coil, wound just outside the NMR chamber, was implanted in epoxy, and did not directly touch the ^{3}He. The Pt wire thermometer (*b*) to measure the temperature of liquid ^{3}He was located at the middle of the NMR tail piece. A pressure gauge (*c*) to measure the pressure of liquid ^{3}He was located at the top of the NMR tail piece.

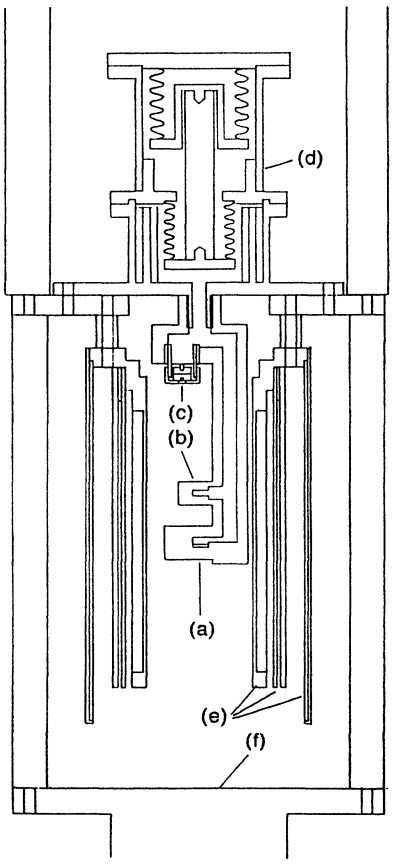

FIG. 1. Schematic drawing of our sample cell and magnet assembly with a superconducting magnetic shield. (a) NMR chamber for solid ^{3}He sample, (b) Pt NMR thermometer. (c) Pressure gauge. (d) Compressional device. (e) Magnet assembly. (f) Nuclear demagnetization stage.

A small superconducting magnet assembly (*e*) produced an applied field, H_0, for NMR experiments. This magnet assembly had a superconducting niobium tube to shield the fringe field of the main magnet of the nuclear refrigerator and the effect of nearby magnetic materials. Inside this shield there were five sets of coils to produce a highly homogeneous magnetic field. One was the main solenoid with outside notches to produce a uniform field along the z axis. The others were compensation coils which could produce $\partial H_z/\partial x$, $\partial H_z/\partial y$, $\partial H_z/\partial z$, and $\partial^2 H_z/\partial z^2$. By adjusting the current separately for these compensation coils we could produce a uniform field whose homogeneity was about 40 ppm at low fields and about 10 ppm at high fields in the sample space for ^{3}He NMR (3 mm $\phi \times 4$ mm length). The size of a solid sample was much smaller than this sample space (the volume of a solid sample was typically 3 mm^3), and thus the effect of field inhomogeneity on the measured linewidth for our samples was negligible. The field gradient coils were also used for the NMR imaging experiments in this work (see Sec. III C). This magnet assembly was thermally anchored to the mixing chamber of the dilution refrigerator and was mechanically supported from the nuclear stage by *TI*-5031 rods[15] which have poor thermal conductivity at very low temperature. The thermal isolation of the magnet assembly from the nuclear stage and the construction of the NMR cell without metallic materials allowed us to sweep the magnetic field even at the lowest temperatures without any disturbance by heating due to flux motion or eddy currents when a field was changed.

The cw-NMR data were taken by the conventional Q-meter method. The inductance of our NMR coil was 39 μH. By using additional capacitors or inductors in the tank circuit at room temperature we could tune the resonance frequency of the tank circuit between 200 kHz and 16 MHz. The cw-NMR signal was obtained by sweeping either the magnetic field or the operating frequency. In general the field-sweep method is more reliable than the frequency-sweep method. When an absorption signal was sharp and large, compared with the base-line change due to the circuit Q value, we measured an absorption spectrum by the frequency-sweep method with good accuracy in a short time. When a signal was broad and weak, the field-sweep method was used, but in this case the measured linewidth had to be converted to a true linewidth by multiplying $\partial\omega/\partial\omega_L$ obtained from Eq. (2). In this

work, the linewidth was defined as a full linewidth of the half-height of the maximum (FWHM).

The solid ^{3}He sample was grown as follows. First we cooled liquid ^{3}He, whose pressure was several hundred mbar below the melting pressure, down to about 0.5 mK. We then pressurized the liquid to 1 mbar above the melting pressure. Soon after that, we applied typically about 1 erg of dc heat through the NMR coil. This heat raised the temperature of the coil itself and the Stycast wall between coil and liquid ^{3}He, and finally raised the temperature of liquid. By this heat pulse we could initiate the growth of solid ^{3}He in the NMR cell. The crystal formed by this method was always in the paramagnetic phase at first. Then the crystal was cooled down to an initial temperature of 0.5 mK at a time constant of about 10 min. After about an hour we melted the crystal until we had a very small seed crystal of about 0.1 mm^3. Then a crystal of about 3 mm^3 was grown under excess pressure of a little less than 1 mbar. After the crystal had grown we checked the line shape of the NMR signal and always found signals from all three kinds of magnetic domains. If one of the signals had a multipeak structure we carefully melted and grew the crystal again until the multipeak structure disappeared. In most cases we could eliminate the multipeak structure by this process. The possible origin of this multipeak structure will be discussed later (Sec. III C). After this annealing process, the line shape became narrow and reproducible. We measured the linewidth and resonance frequency as a function of the external magnetic field and temperature for samples with various orientational angles θ. The orientational angle θ for a sample was determined by fitting the field dependence of the resonance frequency $\omega_{\pm}$ to Eq. (2). We found a small systematic deviation of $\omega_{\pm}$ from Eq. (2), which will be presented in the Appendix. It should be mentioned that the crystal was surrounded by superfluid ^{3}He except for the bottom flat wall, and it was in good thermal contact with the superfluid. It should also be noted that inside the crystal there was no heater wire which could affect the relaxation process in the crystal or the domain distribution.[7] Most of the crystals made by this method had three kinds of magnetic domains except the one shown in Fig. 4, but the size of each domain was of the same order of the crystal size itself as we explain later (Sec. III C), that is, the crystal was usually composed of only three large magnetic domains.

III. EXPERIMENTAL RESULTS

In this section we show some typical results for the field and temperature dependences of the linewidth. In order to investigate some other possible sources of the line-broadening mechanisms, for example, due to a temperature gradient across a sample or due to a magnetic domain boundary scattering of spin waves, we discuss the results of linewidth measurements as a function of sample volume in Sec. III B and the NMR-imaging results for mapping the magnetic domain structure and its size in Sec. III C.

A. Measured linewidth

Figure 2 shows a typical field dependence of the linewidth, which was taken for a sample with $\cos^2\theta=0.22$ at a temperature of $0.68T_N$, where T_N is the transition temperature and is chosen to be 0.93 mK.[16] The linewidth for the upper and lower modes are shown by solid and open circles, respectively. In the upper mode the linewidth decreased monotonically with increasing external magnetic field and became saturated at high fields. In the lower mode, the linewidth decreased very rapidly until the external field corresponding to the Larmor frequency of 500 kHz, denoted by region I in the figure, increased slowly between 500 and 1100 kHz (region II), and then increased rapidly above 1100 kHz (region III). The values for field dividing regions I and II and the field dividing regions II and III are defined as ω_{L1} and ω_{L2}, respectively. Osheroff *et al.* reported similar rapid broadening of the linewidth in the lower mode at ω_{L1}.[1] In Fig. 2, solid and dotted lines are theoretical curves of the linewidth for the upper and lower modes, respectively, which will be discussed in Sec. IV A.

Figure 3 shows similar linewidth data for the same sample as in Fig. 2 at three different temperatures $0.58T_N$, $0.68T_N$, and $0.80T_N$. Figure 3(a) shows data for the upper mode and Fig. 3(b) for the lower mode. As can be seen from the figures, the characteristic features of the field dependence do not change qualitatively by changing the temperature. A few comments on the temperature dependence of the linewidth should be noted here. From Fig. 3(a) the linewidth for the upper mode depended strongly on temperatures at low fields but it became almost constant and did not depend much on temperature at high fields. From Fig. 3(b) the linewidth for the lower mode did not depend much on temperature in region I, but depended strongly on temperature in region II.

For samples with large value of $\cos^2\theta$ (theoretically

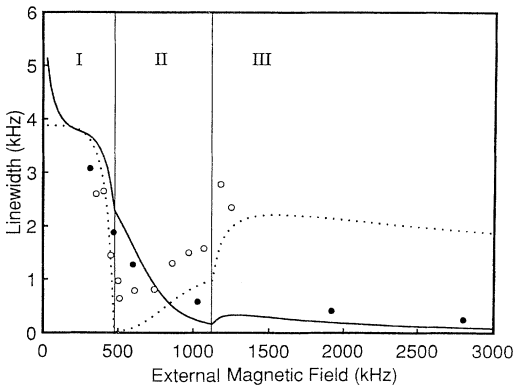

FIG. 2. Typical data of field dependence of the linewidth for a sample with $\cos^2\theta=0.22$ at $T=0.68T_N$. Data for the upper and lower modes are shown by solid and open circles, respectively. Solid and dotted lines are theoretical curves (discussed later). Three regions I, II, and III, and the boundaries, ω_{L1} and ω_{L2}, are shown.

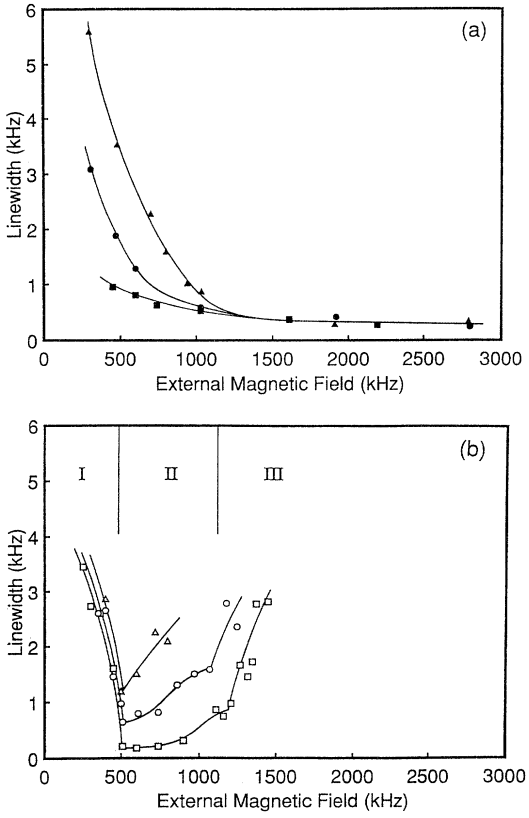

FIG. 3. Field dependence of the linewidth for the same sample as Fig. 2 at various temperatures, $0.58T_N$(■,□), $0.68T_N$(●,○), and $0.80T_N$(▲,△). (a) For upper mode. (b) For lower mode. Solid lines for each temperature are guides for the eyes.

larger than $\frac{9}{25}$, which will be discussed in Sec. IV A), the characteristic features of the field dependence and temperature dependence for the upper mode were essentially the same as that shown in Fig. 3(a), while for the lower mode the linewidth became too broad to observe the NMR signals. It was found that the values of the boundaries, ω_{L1} and ω_{L2}, depended slightly on temperature as shown in Fig. 3(b), and strongly on $\cos^2\theta$. For larger values of $\cos^2\theta$, region II disappeared.

Now we shall discuss data for a peculiar sample with a single magnetic domain. During experimental runs in this work, we found this kind of crystal only once. The crystal did not grow further even when we applied 1 mbar overpressure above the melting pressure for several days. Thus the crystal size was about 0.1 mm^3 (about 30 times smaller than the typical size of 3 mm^3) but was very stable against pressure fluctuation and other disturbances. Figure 4 shows the linewidth for the upper mode of this sample with $\cos^2\theta=0.097$ at $T=0.57T_N$. We could not observe any signals for the lower mode of this sample. The linewidth of Fig 4 was narrower than those of other samples and saturated at about 50 Hz at high fields, probably because $\cos^2\theta$ was very small and the temperature was low (these arguments will be discussed

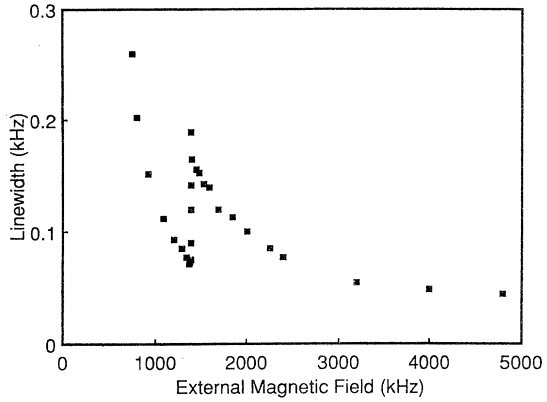

FIG. 4. Field dependence of the linewidth for a special sample which has a single magnetic domain with $\cos^2\theta=0.097$ at $T=0.57T_N$.

in Sec. IV) and the crystal size was small (this will be discussed in Sec. III B). The data clearly shows a rapid increase of the linewidth at around $\omega_L=1400$ kHz. This value of ω_L will be referred to as ω_{L2} in the later discussion. Since this crystal was special, we will not include this data in our analysis, hereafter.

B. Sample volume dependence of the linewidth

We measured the volume dependence of the linewidth and resonance frequency for a sample with a particular value of $\cos^2\theta$ at a fixed external field. Figure 5(a) shows the volume dependence of the linewidth of the upper mode for $\cos^2\theta=0.41$ at $T=0.55T_N$. The horizontal axis of this figure is actually a signal intensity, but we converted it to the volume of the sample using the calibrated NMR sensitivity to within about 10% accuracy. The linewidth increased with increasing sample volume. Figure 5(b) shows the volume dependence of the central frequency of an absorption signal for the same sample. The central frequency decreased with increasing sample volume.

Among several mechanisms which might give a volume dependent linewidth, one plausible explanation for the data of Fig. 5 is the effect of a temperature gradient across the sample. Our sample of solid ^{3}He was sitting on the bottom of the sample cell. This sample cell was made of Stycast, which is known to release time-dependent heat.[17] There should be a heat current from the cell wall through the sample toward the surrounding superfluid ^{3}He, whose temperature was firmly fixed to the nuclear refrigerator. This heat flow gives rise to the temperature gradient across the sample and thus to the distribution of the local antiferromagnetic resonance frequency, $\Omega_0(T)$. The estimated heat flow from the observed slope of the linewidth versus volume was in the order of 0.1 pW, when the data of thermal conductivity measured by Feng *et al.*[18] was used.

Since the observed volume dependence of the linewidth may be of extrinsic origin, we have to exclude this effect

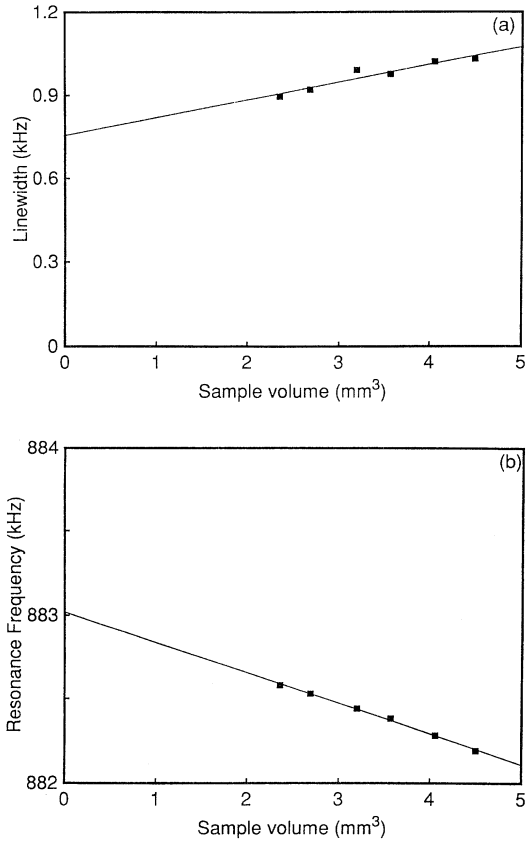

FIG. 5. Typical data of the volume dependence of linewidth (a) and the center frequency of resonance (b) for a sample with $\cos^2\theta=0.41$ at $T=0.55T_N$. Straight lines are guides for the eyes.

by reducing the sample volume while maintaining a good signal to noise ratio. Thus we chose a volume of 3 mm^3 for the sample so that we have enough sensitivity to all signals from three domains for the entire range of the external magnetic field. This extra broadening due to the finite volume of the sample depended on the external field, but gave at most a 20% contribution to the total measured linewidth for our measured region of the field.

C. Domain structure and its distribution

We performed an NMR imaging experiment to find the magnetic domain structure and its size in a single crystal sample, because the size and structure of the domains were very important to estimate the contribution of two-magnon and spin diffusion processes to the relaxation mechanism. Most of the crystals of antiferromagnetic solid ^{3}He which have been made so far, i.e., those in this work, by Osheroff *et al.*,[1] Kusomoto *et al.*,[7] and Feng *et al.*,[18] contained three kinds of magnetic domains in a single crystal. Feng *et al.*[18] made a crystal, 95% of whose volume was made of one magnetic domain, by the method of quasi-one-dimensional growth of the crystal,

FIG. 6. Typical cw-NMR spectrum for a sample with a multipeak structure, $C1$ and $C2$, besides the usual A and B domain signals.

but their seed crystal still contained three magnetic domains. There is no obvious reason why an antiferromagnetic single crystal has a multidomain structure.

In the present NMR imaging experiment we used a cw-NMR method.[13] We measured the resonance frequency and linewidth for the linear field gradient applied along three principal axes in the laboratory frame. In this case the center frequency of the resonance absorption spectrum gives information on the position of the magnetic domain, while the linewidth gives that of the domain size.

After the first formation of the solid ^{3}He by a heat pulse, there sometimes appeared an NMR signal where each domain showed a multipeak structure. One example is shown as $C1$ and $C2$ in Fig. 6. We applied our NMR imaging technique to this sample. As a result we obtained the distribution of the domains as shown in Fig. 7. As can be seen from the figure, the sample of the present example was composed of four large domains (A, B, $C1$ and $C2$). Moreover, it can be seen that between domains $C1$ and $C2$ there were the two domains of A and B. Since the domain sizes were large, the two-magnon relaxation process due to the domain boundary may be negligible.[11]

The difference between the resonance frequencies of $C1$ and $C2$ might be explained by a possible lattice distortion due to magnetostriction. Because of the uniaxial anisotropy in the antiferromagnetic phase, the lattice constant along the l vector, c, and that for perpendicular direction, a, might be different and the lattice distortion, ϵ, is $|c/a-1|$. Also from theoretical considerations it has

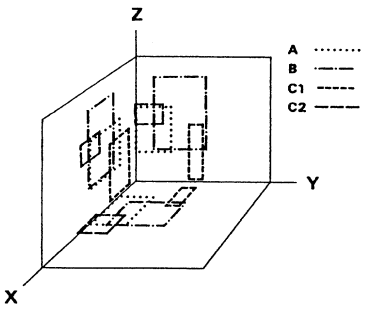

FIG. 7. Distribution of magnetic domains, A, B, $C1$, and $C2$ in a single crystal sample. The boxes shown in X-Y and other planes indicate the size (not the actual domain shape) and locations of each domain projected on the planes.

been shown that the domain wall in the $U2D2$ phase would be in the (110) or its equivalent planes.[11] Then we expect there are twin structures in this phase. In this situation two magnetic domains of the same kind (say, domains $C1$ and $C2$), which have other magnetic domain(s) between them, may have slightly different directions. For instance, if there is one domain B between $C1$ and $C2$, the frequency splitting between $C1$ and $C2$ can be related to ϵ as follows:

$$|\cos^2\theta_{C1}-\cos^2\theta_{C2}| \simeq 4\cos\theta_C\cos\theta_B\epsilon \ . \tag{3a}$$

If there are two domains, A and B, between $C1$ and $C2$,

$$|\cos^2\theta_{C1}-\cos^2\theta_{C2}| \simeq 2\cos\theta_C|\cos\theta_A \pm \cos\theta_B|\epsilon \ . \tag{3b}$$

Thus, for the example of Fig. 6, a value of $\epsilon=|c/a-1|$ of the order of 10^{-3} may explain the observed splitting. This distortion agrees with the rough estimate resulting from the balance of elastic energy $(\frac{1}{2})(m_3/2\omega_D^2)(a\epsilon)^2$ and the exchange energy $3\gamma_G\epsilon J$, where the atomic mass of ^{3}He, m_3, is 5×10^{-24} g, the Debye frequency, ω_D, 2×10^{12} sec^{-1}, the lattice constant, a, 3×10^{-8} cm, the exchange energy, J, 10^{-3} k_B (erg), and the Grüneisen constant, γ_G, is 18.

This rather large magnetostriction might cause a distortion around the nucleation seed of the crystal which might create the multidomain structure and maintain a memory of the three domain structures. To check this hypothesis we made a test as follows. First we measured the domain distribution by the above-mentioned imaging technique. We slowly raised the magnetic field until the sample entered the high-field phase. After the whole system achieved equilibrium, we decreased the magnetic field down to the original value in the low-field phase. Then we measured the distribution of the magnetic domains again. We found three domains again but the distribution had changed from the original one. This result clearly showed that the domain distribution was not affected by the distortion of the lattice. Another possibility may be the boundary effect between solid and liquid, that is, there might be some orientation effect on the anisotropy axis l at the boundary. If this is the case we can never have a monodomain sample if the solid sample is located in liquid.

IV. THEORY OF MULTIMAGNON RELAXATION RATE AND COMPARISON WITH EXPERIMENT

A. Theory

The low-lying excitations of the antiferromagnetic material at very low temperatures are well described by magnons where the energy and momentum of the magnon are expressed by $\epsilon(\mathbf{k})$ and $\mathbf{k}$. According to the magnon picture for the relaxation processes of cw-NMR, we first excite magnons with $\mathbf{k}=\mathbf{0}$ which decay into magnons with $\mathbf{k}\neq\mathbf{0}$. Since $\tau\omega_{\pm}\gg1$, where τ is the inverse of linewidth, the relaxation process can be regarded as the collisionless limit and thus the transition probability of $\mathbf{k}=\mathbf{0}$ magnon to other $\mathbf{k}\neq\mathbf{0}$ magnons should be directly related to the observed linewidth.

At very low temperatures, the relaxation processes should be attributed to the lower-order magnon processes, i.e., two-, three-, and four-magnon processes. In these elementary processes, total energy and total momentum should be conserved for each process. The two-magnon relaxation process is effective only if there are some inelastic scattering centers within a crystal, for example, crystal defects, magnetic domain walls or magnetic stacking defects caused by dislocations.[19] Such two-magnon processes may be independent of temperature or mildly depend on temperature.

Figure 8(a) shows a schematic diagram of the three-magnon process in the upper mode. A $\mathbf{k}=\mathbf{0}$ magnon in the upper mode splits into two magnons in the lower mode whose momenta are $\mathbf{k}$ and $-\mathbf{k}$ for momentum conservation. In order to satisfy the energy conservation law, the following condition has to be satisfied:

$$\omega_+ > 2\omega_- \ . \tag{4}$$

Thus, in general, when we observe the linewidth as a function of applied field, there exist two values of fields, ω_{L1} and ω_{L2}, which satisfy $\omega_+=2\omega_-$ and in the region

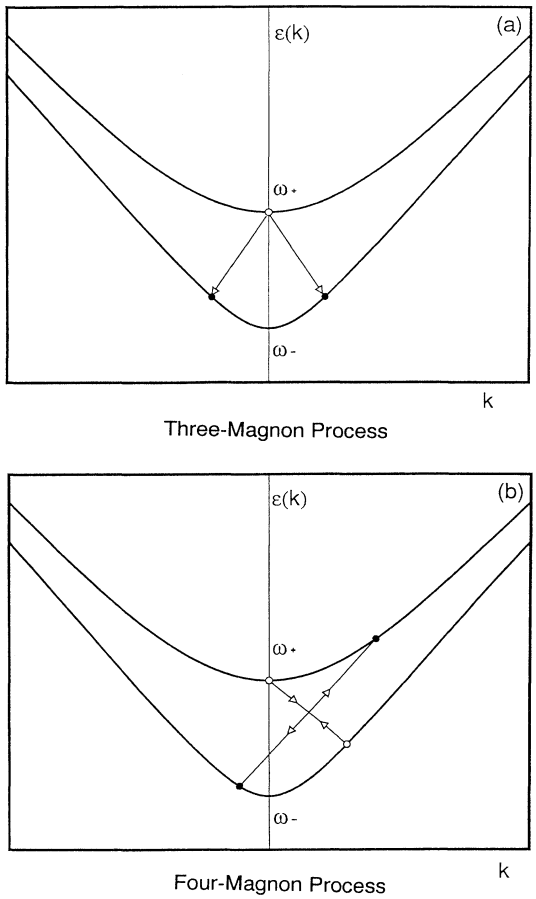

FIG. 8. Schematic diagram of a three-magnon process (a) and one of four magnon-processes (b) for the decay of a uniform mode ($k=0$ magnon) in the upper mode.

between ω_{L1} and ω_{L2} (region II in Fig. 2) the three-magnon process is forbidden. These values of ω_{L1} and ω_{L2} can be solved easily from Eq. (2) as follows:

$$\left.\begin{matrix}\omega_{L1}\\ \omega_{L2}\end{matrix}\right\} = \frac{\Omega_0(T)}{4}(5\sqrt{1-\cos^2\theta} \mp \sqrt{9-25\cos^2\theta}) \ . \quad (5)$$

These values of ω_{L1} and ω_{L2} depend on temperature through $\Omega_0(T)$ and on $\cos^2\theta$. It should be noted that there is no three-magnon forbidden region for $\cos^2\theta \geq 9/25$. On the contrary, the four-magnon process, one of whose diagrams for the upper mode is shown in Fig. 8(b), does not have any forbidden region in fields. The four-magnon process should be a dominant relaxation process at least in the three-magnon forbidden region.

Recently Ohmi and Tsubota (OT)[20] calculated the spin relaxation rate due to three- and four-magnon processes. They first generalized the effective Hamiltonian which describes the spin dynamics to include long-wavelength magnons with a continuum approximation as follows:

$$H = \frac{\gamma^2}{2\chi}\mathbf{S}\cdot\mathbf{S} - \gamma\mathbf{S}\cdot\mathbf{H}_0 + \frac{\chi}{2\gamma^2}\cdot\Omega_0^2(\hat{\mathbf{d}}\cdot\boldsymbol{l})^2 + \frac{\chi}{2\gamma^2}[(C_\perp\nabla_\perp\cdot\hat{\mathbf{d}})^2 + (C_\parallel\nabla_\parallel\cdot\hat{\mathbf{d}})^2] \ , \quad (6)$$

where $C_\perp$ and $C_\parallel$ are the spin-wave velocities perpendicular and parallel to $\boldsymbol{l}$, respectively. From this Hamiltonian together with the following commutation relations:

$$[S_i, S_j] = i\epsilon_{ijk}\hbar S_k \ , \quad (7a)$$

$$[S_i, d_j] = i\epsilon_{ijk}\hbar d_k \ , \quad (7b)$$

they obtained the following equations of motion for $\mathbf{S}$ and $\hat{\mathbf{d}}$:

$$\dot{\mathbf{S}} = \gamma\mathbf{S}\times\mathbf{H}_0 - \frac{\chi}{\gamma^2}\Omega_0^2(\hat{\mathbf{d}}\cdot\boldsymbol{l})(\hat{\mathbf{d}}\times\boldsymbol{l}) + \frac{\chi}{\gamma^2}\hat{\mathbf{d}}\times[C_\perp^2\nabla_\perp^2\hat{\mathbf{d}} + C_\parallel^2\nabla_\parallel^2\hat{\mathbf{d}}] \ , \quad (8a)$$

$$\dot{\hat{\mathbf{d}}} = \gamma\hat{\mathbf{d}}\times\left[\mathbf{H}_0 - \frac{\gamma}{\chi}\mathbf{S}\right] \ . \quad (8b)$$

These are a generalization of the OCF equations. Then, starting from the Hamiltonian of Eq. (6), OT derived the multimagnon Hamiltonian with the use of the Holstein-Primakoff method. They calculated the life time of the $\mathbf{k}=\mathbf{0}$ mode magnon from the multimagnon Hamiltonian. They obtained results for the three- and four-magnon relaxation rate, $\Gamma_\pm^{(3)}$ and $\Gamma_\pm^{(4)}$ where $\pm$ denotes the upper and lower modes, respectively,

$$\Gamma_+^{(3)} = \frac{v^2\gamma^2\omega_L^2}{2\pi^2\chi C^3\omega_+}\left[\left[\frac{\omega_+}{2}\right]^2 - \omega_-^2\right]^{1/2} k_B T \ , \quad (9a)$$

$$\Gamma_-^{(3)} = \frac{v^2\gamma^2\omega_L^2\omega_+^3}{8\pi^2\chi C^3\omega_-^2}\frac{\left[\left[\frac{\omega_+}{2}\right]^2 - \omega_-^2\right]^{1/2}}{\frac{\omega_+^2}{2} - \omega_-^2} k_B T \ , \quad (9b)$$

$$\Gamma_+^{(4)} = \frac{(\gamma^2/\chi)^2}{2(2\pi)^4\hbar C^6}\left[1 - u^2\frac{\omega_L^2}{\omega_+^2}\right]^2\omega_+^2 \times[\tfrac{2}{3}\pi^2\ln(k_B T/\hbar\omega_-) + 0.7](k_B T)^3 \ , \quad (9c)$$

$$\Gamma_-^{(4)} = \frac{(\gamma^2/\chi)^2}{2(2\pi)^4\hbar C^6}\left[1 - v^2\frac{\omega_L^2}{\omega_-^2}\right]^2\omega_-^2 \times[\tfrac{2}{3}\pi^2\ln(k_B T/\hbar\omega_+) + 0.7](k_B T)^3 \ , \quad (9d)$$

where

$$\left.\begin{matrix}u^2\\ v^2\end{matrix}\right\} = \frac{1}{2}\left[1 \pm \frac{\omega_L^2 + \Omega_0^2(2\cos^2\theta - 1)}{\sqrt{(\omega_L^2 - \Omega_0^2)^2 + 4\omega_L^2\Omega_0^2\cos^2\theta}}\right] \quad (10)$$

and C is an averaged spin wave velocity given by

$$C = (C_\perp^2 C_\parallel)^{1/3} \quad (11)$$

and $\omega_\pm$ is given by Eq. (2). Thus, the total linewidth due to three- and four-magnon processes is given by

$$\Gamma_\pm = \Gamma_\pm^{(3)} + \Gamma_\pm^{(4)} \ . \quad (12)$$

Figure 9 shows the field dependence of the calculated total linewidth $\Gamma_\pm$ for $\cos^2\theta = 0.2$ [Figs. 9(a) and 9(b)], and for $\cos^2\theta = 0.8$ [Figs. 9(c) and 9(d)] at $T = 0.5T_N$, $0.7T_N$, using the experimentally determined parameters $\chi^{-1} = 0.185\times10^6$ cgs,[4] $c = 7.7$ cm/sec,[5] $T_N = 0.93$ mK,[16] $\gamma = 2.04\times10^4$ $G^{-1}\text{sec}^{-1}$. We used measured values of $(\Omega_0/2\pi)^2 = 5.9\times10^{11}$ kHz^2 at $T = 0.5T_N$, and 5.0×10^{11} kHz^2 at $T = 0.7T_N$. It should be mentioned that all physical quantities in Eqs. (9)–(12) were measured and there was no fitting parameter. Figures 9(a) and 9(b) are for $\cos^2\theta = 0.2$ where the three-magnon forbidden region exists. The three-magnon forbidden region is indicated in the figures by ω_{L1} and ω_{L2} for $T = 0.5T_N$. Figures 9(c) and 9(d) are for $\cos^2\theta = 0.8$ where the three-magnon process is operative for the entire fields. The heavy lines are the total linewidth given by Eq. (12) and the fine lines show the contribution from the four-magnon process. Thus, the difference between these lines corresponds to the contribution due to the three-magnon process.

In the upper mode, the four-magnon process gives a major contribution to the linewidth in the entire temperature range we observed. By this process the linewidth decreases with increasing external magnetic field except for small humps outside of the three-magnon forbidden region in the case of $\cos^2\theta = 0.2$ [Fig. 9(a)]. Within the three-magnon forbidden region (region II) only the four-magnon process is operative. When $\cos^2\theta = 0.8$ [Fig. 9(c)], the three-magnon process is allowed for the entire field region and thus total linewidth decreases smoothly with increasing external magnetic field.

In the lower mode there is a steep change of the linewidth near ω_{L1} and ω_{L2} in the case of $\cos^2\theta = 0.2$ [Fig. 9(b)]. In the three-magnon forbidden region the four-magnon process again governs the relaxation and the linewidth increases with increasing external magnetic field. When $\cos^2\theta = 0.8$ [Fig. 9(d)], there is no steep change of the linewidth. The total linewidth decreases

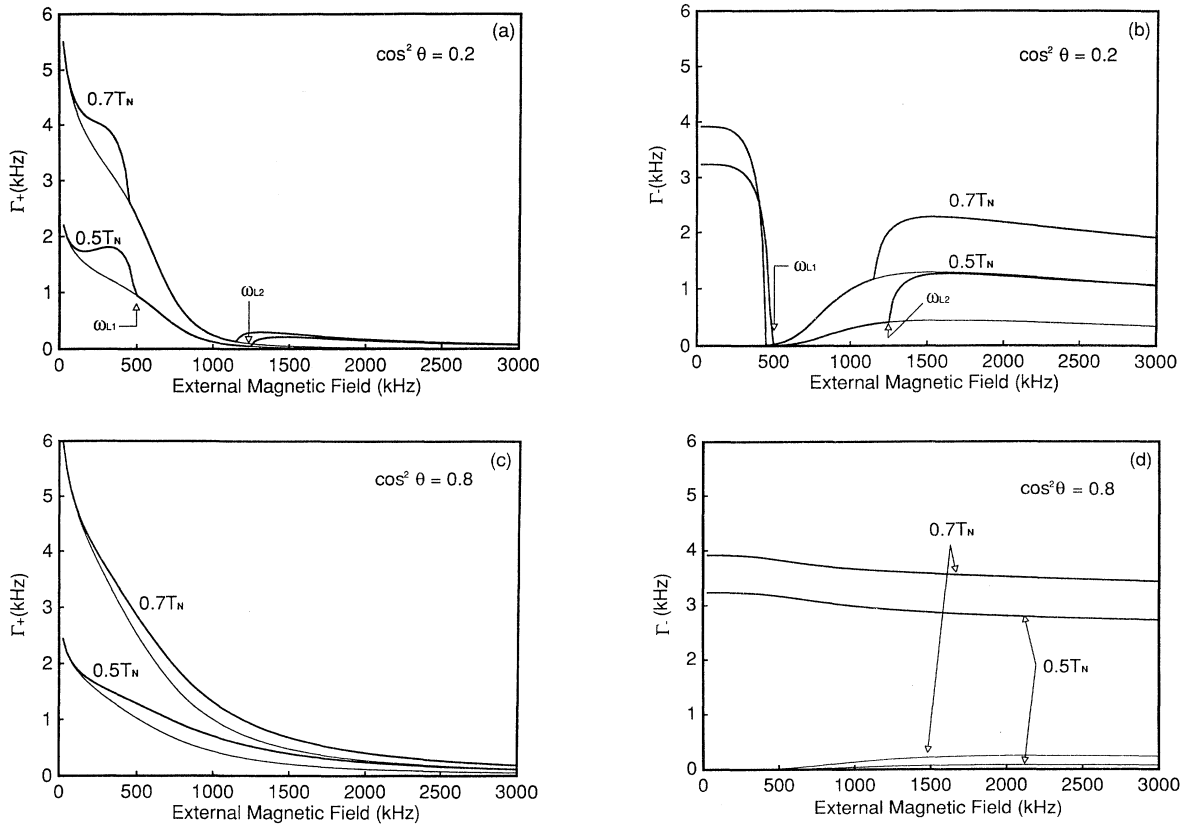

FIG. 9. Theoretical curves of the field dependence of the linewidth at $T=0.5T_N$ and $0.7T_N$. The heavy solid lines are the total linewidth due to the three- and four-magnon processes, and the thin solid lines show contributions from the four magnon process. (a) For the upper mode with $\cos^2\theta=0.2$; (b) for the lower mode with $\cos^2\theta=0.2$; (c) for the upper mode with $\cos^2\theta=0.8$; (d) for the lower mode with $\cos^2\theta=0.8$.

gradually with increasing external magnetic field. The value of the linewidth is rather large for the entire field region, typically several kHz.

B. Comparison of theory with experiment

Since the OT theory has no adjustable parameters we can compare our experimental results without any fitting procedures. Figure 2 shows a comparison of the observed linewidth with the theory for $\cos^2\theta=0.22$ and $T=0.68T_N$. The general features of both the field dependence and the magnitude of linewidth agree well. It should be noted that the three-magnon forbidden region is clearly seen in the lower mode and the values of ω_{L1} and ω_{L2} calculated by Eq. (5) agree very well with the observed sharp change of the linewidth due to the onset of the three-magnon process.

But there still exists a small difference between theory and experiment. The disagreement is rather noticeable in the upper mode at high fields; that is, the linewidth approaches a constant value instead of decreasing monotonically as the field increases [Fig. 3(a)]. This constant value of the linewidth at high field implies that there exists some other relaxation mechanisms which does not depend much on the field. This excess relaxation mechanism, $\Gamma^{(0)}$, may also be responsible for disagreement of the linewidth in the lower mode in the three-magnon forbidden region.

Here, we introduce $\Gamma^{(0)}$ as a fitting parameter to compare our data with the theory. In order to test the theoretical prediction for the four-magnon process, we analyzed the field dependence of the linewidth in the upper mode only in the three-magnon forbidden region. We fitted our data at various temperatures to the theory for several samples which had $\cos^2\theta<\frac{9}{25}$ by introducing two parameters as follows:

$$\Gamma^{+}_{\rm obs}=A^{(4)}\Gamma^{(4)}_{+}+\Gamma^{(0)} \quad \text{in region } II \ . \tag{13}$$

Here $A^{(4)}$ and $\Gamma^{(0)}$ are the phenomenological parameters which are assumed to be independent of the external magnetic field. Figure 10 shows $A^{(4)}$ and $\Gamma^{(0)}$ as a function of temperature for several samples. The OT theory agreed with our experimental results within a factor of 2 at low temperatures but $A^{(4)}$ depended on temperature. The $\Gamma^{(0)}$ also depended on temperature. Possible mechanisms for the excess linewidth, $\Gamma^{(0)}$, will be discussed in Sec. V.

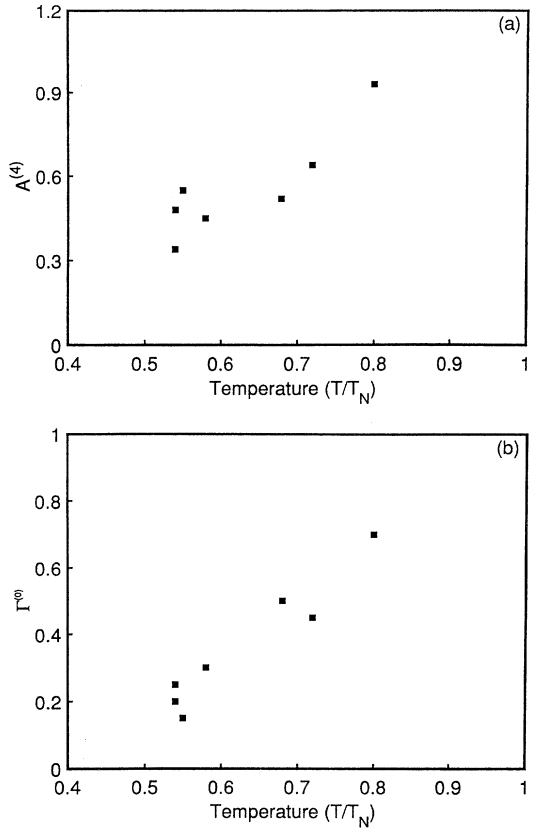

FIG. 10. Fitted values of $A^{(4)}$ and $\Gamma^{(0)}$ are plotted against temperature for various samples with $\cos^2\theta < \frac{9}{25}$.

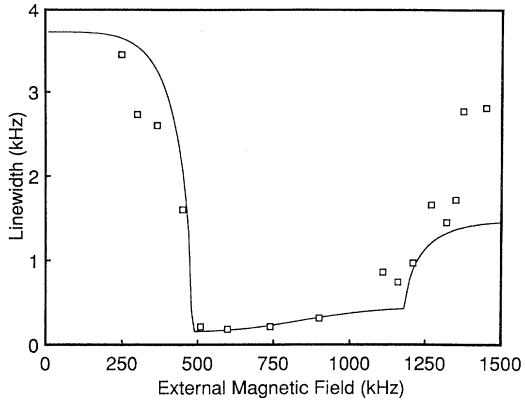

FIG. 11. Fit of theoretical curve to the experimental data of the lower mode for $\cos^2\theta=0.22$ (same as Fig. 2) at $T=0.58T_N$ for $\Gamma^{-}_{\rm obs}=\Gamma^{(3)}_{-}+A^{(4)}\Gamma^{(4)}_{-}+\Gamma^{(0)}$, with the fitted values of parameters; $A^{(4)}=0.45$ and $\Gamma^{(0)}=150$ Hz.

In order to see the consistency of the fitting procedure between the upper and lower modes, and to compare the contribution of the three-magnon process which is dominant in regions I and III of the lower mode, Fig. 11 shows the theoretical curve for the linewidth of the lower mode, using the same values of $A^{(4)}$ as that of the upper mode of the same sample and $\Gamma^{(0)}$ as a free parameter, which is different from that of the upper mode:

$$\Gamma^{-}_{\rm obs}=\Gamma^{(3)}_{-}+A^{(4)}\Gamma^{(4)}_{-}+\Gamma^{(0)} . \tag{14}$$

The theory agreed well with our data in the lower mode.

The field dependence of the linewidth in the upper mode for samples with $\cos^2\theta > \frac{9}{25}$ agreed qualitatively with the theory.

We could not observe a signal in the lower mode for samples with $\cos^2\theta > \frac{9}{25}$. This is consistent with the theoretical prediction that the linewidth in the lower mode is very wide for these samples, since the three-magnon relaxation process is operative for the entire field region. Besides, the resonance frequency is low at low fields and the signal is mainly a longitudinal mode at high fields.

We did not observe any noticeable humps in the upper mode just outside the three-magnon forbidden region except for the sample shown in Fig. 4. This may be partly because the linewidth is mainly determined by the four-magnon process, and we did not have enough data or accuracy in the linewidth measurement to distinguish this hump. This hump was clearly seen for the sample shown in Fig. 4, probably because the observed linewidth was rather narrow for all the regions and the small contribution due to the onset of the three-magnon process was emphasized at ω_{L2}. However, the observed change of the linewidth near ω_{L2} was very sharp and the field dependence did not completely agree with the theory even for this sample.

V. DISCUSSIONS

In the analysis of Sec. IV B we introduced $\Gamma^{(0)}$ which is assumed to be independent of field. This assumption of the field independence of $\Gamma^{(0)}$ may cause some error in determination of $A^{(4)}$. First, we discuss some mechanisms which may contribute to $\Gamma^{(0)}$ and then consider the effect of the field dependence of $\Gamma^{(0)}$ on determination of $A^{(4)}$, if there is any effect.

One of the mechanisms for $\Gamma^{(0)}$ is due to a temperature gradient across the samples as discussed in Sec. III B. This extrinsic linewidth $\Gamma_{\Delta T}$ was always included in our data and was at most 20% of the total measured linewidth. This $\Gamma_{\Delta T}$ arises from the temperature dependence of $\Omega_0(T)$ and thus the field dependence of $\Gamma_{\Delta T}$ should be

$$\Gamma_{\Delta T}\sim\left[\frac{\partial\Omega_0(T)}{\partial T}\right]\cdot\Delta T \quad \text{for } \omega_L \ll \Omega_0 , \tag{15}$$

$$\Gamma_{\Delta T}\sim\frac{\Omega_0(T)}{\omega_L}\left[\frac{\partial\Omega_0(T)}{\partial T}\right]\cos^2\theta\Delta T \quad \text{for } \omega_L \gg \Omega_0 . \tag{16}$$

This field dependence of $\Gamma_{\Delta T}$ was confirmed qualitatively by taking the slope of the volume-dependent linewidth such as Fig. 5 as a function of field at the lowest temperature of $0.5T_N$. If this field dependence of $\Gamma_{\Delta T}$ is subtract-

ed from our measured linewidth, the corrected values of $A^{(4)}$ become smaller than those shown in Fig. 10(a). According to the temperature dependence of the thermal conductivity,[18] $\Gamma_{\Delta T}$ becomes larger in higher temperatures and this might contribute to the positive temperature dependence of $A^{(4)}$. However, we could not take data of the volume dependence of the linewidth at higher temperatures and could not confirm quantitatively the effect of $\Gamma_{\Delta T}$ on $A^{(4)}$.

We believe that some other mechanisms should exist for $\Gamma^{(0)}$ besides $\Gamma_{\Delta T}$ since $\Gamma_{\Delta T}$ should be negligible for the sample in Fig. 4, for example. Another candidate for $\Gamma^{(0)}$ may be due to the two-magnon process $\Gamma^{(2)}$ which requires some scattering centers. We know our sample was a single crystal and the sizes of crystal and magnetic domains in our samples were found to be large. It seems unlikely that the surface of the crystal and domain boundaries would contribute to $\Gamma^{(0)}$, when a measured value of the spin wave velocity of ~ 10 cm/sec was used. Since we do not have any information on what type of magnetic defects there are in our crystal and there is no theory of two-magnon relaxation for any specific magnetic defect, further discussion is postponed.

The demagnetization field due to the large susceptibility might give an extrinsic linewidth of order $10^{-4}\,\omega_L$ at most depending on the sample shape, and contribute to $\Gamma^{(0)}$. If this effect is eliminated from the measured linewidth, the value of $A^{(4)}$ becomes larger than those presented in Sec. IV B, but this broadening mechanism seems to be too small to account for the disagreement between our experiment and theory. This effect is temperature independent and thus this does not explain the temperature dependence of $A^{(4)}$.

In the theory OT stopped the Holstein-Primakoff expansion at the fourth-order term. They claimed that at high temperatures a higher order process such as a five-magnon process is important and also the magnons near the Brillouin zone boundary are thermally excited and these two effects would lead to a temperature dependence of $\Gamma^{(4)}$ higher than T^3. All these effects neglected in the theory may explain the temperature dependence of $A^{(4)}$.

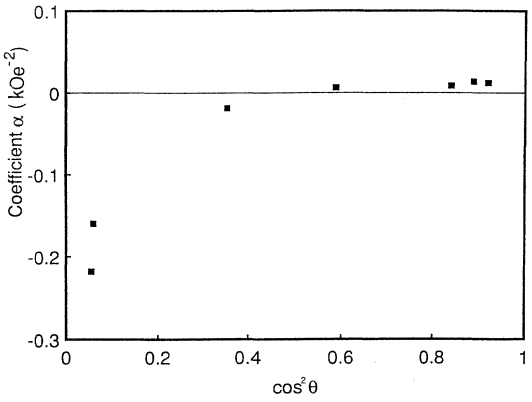

FIG. 13. The fitted values of α in Eq. (A1) (see text) are plotted against $\cos^2\theta$ at $T=0.54T_N$.

ACKNOWLEDGMENTS

We would like to thank Professor T. Tsuneto, Professor T. Ohmi, and Professor M. Tsubota for many stimulating discussions. This work was partly supported by a Grant-in-Aid for the Promotion of Science from the Ministry of Education, Science and Culture, Japan.

APPENDIX

During the course of this work we observed the resonance frequency as a function of a field and determined $\cos^2\theta$ by using Eq. (2). However, the observed field dependence of the resonance frequency could not be fitted to Eq. (2) perfectly and sometimes we observed a negative shift. The negative shift was first reported by Osheroff.[21] Here, we describe this disagreement which may sometimes cause some error in the determination of $\cos^2\theta$, especially when its value is small.

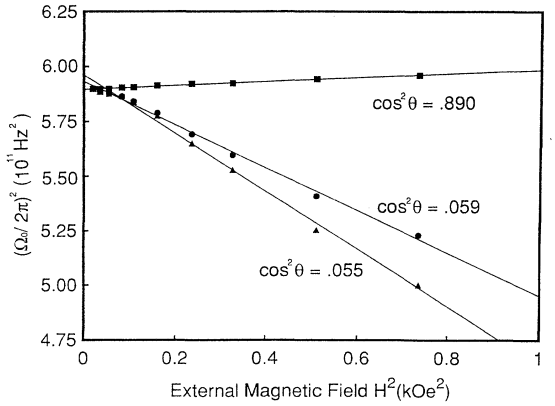

FIG. 12. Field dependence of the values of Ω_0^2 for several values of $\cos^2\theta$ at $T=0.54T_N$.

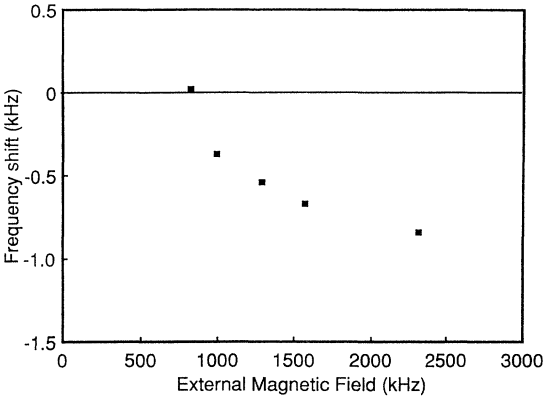

FIG. 14 Field dependence of the observed negative shift (from the Larmor frequency) of the resonance frequency for a sample with a small value of $\cos^2\theta \simeq 10^{-3}$ at $T=0.55T_N$.

1. Field dependence of the antiferromagnetic frequency Ω_0

Equation (2) explains the global behavior of the NMR spectrum well, where Ω_0^2 and $\cos^2\theta$ are assumed to be independent of the field.[1] The fitting of Eq. (2) to the measured data set (ω_L, ω) showed small systematic errors. To eliminate these systematic errors we have to introduce a field-dependent antiferromagnetic frequency $\Omega_0(H)$ as follows:

$$\Omega_0^2(H)=\Omega_0^2(0)(1+\alpha H^2) , \quad \text{(A1)}$$

where $\Omega_0^2(0)$ and α are field independent. Combining Eqs. (2) and (A1) we can make a good fit to our data sets for $H<1$ kOe. Figure 12 shows some examples of the fitted values of $\Omega_0^2(H)$ as a function of H^2 at $T=0.54T_N$. As can be seen, $\Omega_0^2(H)$ has strong field dependence, especially when $\cos^2\theta$ is small. Figure 13 shows the $\cos^2\theta$ dependence of the coefficient α at $T=0.54T_N$. The quantity α is positive and is of order 10^{-2} kOe^{-2} when $\cos^2\theta\simeq 1$, but α decreases with decreasing $\cos^2\theta$. When $\cos^2\theta\simeq 0$, α is negative and is of order 10^{-1} kOe^{-2}. This large value of $|\alpha|$ for small $\cos^2\theta$ is unacceptable because it gives zero or negative value to $\Omega_0^2(H)$ if we extrapolate Eq. (A1) to $H=4$ kOe.

2. Negative frequency shift

Figure 14 shows a negatively shifted resonance frequency from ω_L taken for the sample with $\cos^2\theta\simeq 10^{-3}$ at $T=0.55T_N$. This negative shift cannot be explained by the demagnetization field due to the large susceptibility of this antiferromagnetic phase, since its negative frequency shift may be of the order of $7\times 10^{-5}\,\omega_L$ at most, and was too small to explain the experimental data. This negative frequency shift seems to saturate at around 1 kHz in the high-field region as shown in Fig. 14. Perhaps there should be another torque term in the equations of motion (1) which might give nearly constant negative shift.

[1] D. D. Osheroff, M. C. Cross, and D. S. Fisher, Phys. Rev. Lett. **44**, 792 (1980).

[2] A. Benoit, J. Bossy, J. Flouquet, and J. Schweizer, J. Phys. Lett. **46**, L923 (1985).

[3] See, e.g., M. Roger, J. H. Hetherington, and J. M. Delrieu, Rev. Mod. Phys. **55**, 1 (1983); D. M. Ceperley and G. Jacucci, Phys. Rev. Lett. **58**, 1648 (1987).

[4] D. D. Osheroff, H. Godfrin, and R. Ruel, Phys. Rev. Lett. **58**, 2458 (1987); T. Hata, S. Yamazaki, M. Takeda, T. Kodama, and T. Shigi, *ibid.* **51**, 1573 (1983).

[5] D. D. Osheroff and C. Yu, Phys. Lett. A **77**, 458 (1980).

[6] See, e.g., O. V. Lounasmaa, Physics Today **26**(10), 26 (1989).

[7] T. Kusumoto, O. Ishikawa, T. Mizusaki, and A. Hirai, J. Low. Temp. Phys. **59**, 269 (1985).

[8] M. Tsubota and T. Tsuneto, in *Proceedings of the 17th International Conference on Low Temperature Physics, Karlsruhe, 1984,* edited by U. Eckern, A. Schmid, W. Weber, and H. Wühl (North-Holland, Amsterdam, 1984), Vol. 1, p. 241.

[9] M. Tsubota, Prog. Theor. Phys. **79**, 47 (1988).

[10] T. Ohmi, M. Tsubota, and T. Tsuneto, Prog. Theor. Phys. **73**, 1075 (1985).

[11] M. Tsubota, T. Ohmi, and T. Tsuneto, Prog. Theor. Phys. **76**, 1222 (1986).

[12] Y. Sasaki, K. Sasayama, T. Mizusaki, and A. Hirai, Jpn. J. Appl. Phys. Suppl. **26-3**, 417 (1987).

[13] Y. Sasaki, Y. Hara, T. Mizusaki, and A. Hirai, in *Symposium on Quantum Fluids and Solids—1989,* Proceedings of the Conference on Quantum Fluids and Solids—1989, University of Florida, Gainesville, Florida, AIP Conf. Proc. No. 194, edited by Gary G. Ihas and Yasumasa Takano (AIP, New York, 1989), p. 286.

[14] Y. Sasaki, Y. Hara, T. Mizusaki, and A. Hirai, Physica B **165&166**, 801 (1990).

[15] TI-5031 (Torey, Co., Japan). Thermal conductivity of this material was measured to be $\kappa=1.5\times 10^{-2}\,T^{1.7}$ W/m K at very low temperatures.

[16] D. S. Greywall and P. A. Bush, Phys. Rev. B **36**, 6853 (1987); D. S. Greywall, *ibid.* **33**, 7520 (1986).

[17] M. Schwark, F. Pobell, M. Kubota, and R. M. Mueller, J. Low Temp. Phys. **58**, 171 (1985).

[18] Y. P. Feng, P. Schiffer, J. Mihalisin, and D. D. Osheroff, Phys. Rev. Lett. **65**, 1450 (1990).

[19] D. D. Osheroff (private communication).

[20] T. Ohmi and M. Tsubota, J. Low Temp. Phys. **83**, 177 (1991).

[21] D. D. Osheroff, Physica B **109&110**, 1461 (1982).